

Fabrication of a Microcavity Prepared by Remote Epitaxy over Monolayer Molybdenum Disulfide

Yeonhoo Kim, John Watt, Xuedan Ma, Towfiq Ahmed, Suhyun Kim, Kibum Kang, Ting S. Luk, Young Joon Hong, and Jinkyong Yoo*

Cite This: <https://doi.org/10.1021/acsnano.1c08779>

Read Online

ACCESS |

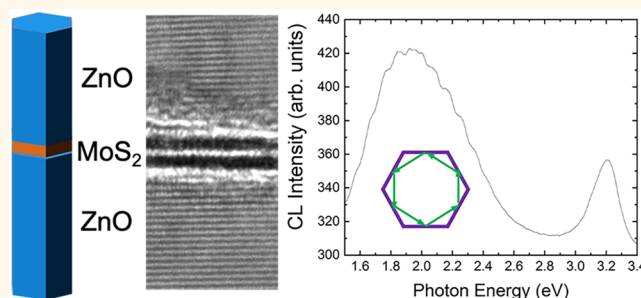
Metrics & More

Article Recommendations

Supporting Information

ABSTRACT: Advances in epitaxy have enabled the preparation of high-quality material architectures consisting of incommensurate components. Remote epitaxy based on lattice transparency of atomically thin graphene has been intensively studied for cost-effective advanced device manufacturing and heterostructure formation. However, remote epitaxy on nongraphene two-dimensional (2D) materials has rarely been studied even though it has a broad and immediate impact on various disciplines, such as many-body physics and the design of advanced devices. Herein, we report remote epitaxy of ZnO on monolayer MoS₂ and the realization of a whispering-gallery-mode (WGM) cavity composed of a single crystalline ZnO nanorod and monolayer MoS₂. Cross-sectional transmission electron microscopy and first-principles calculations revealed that the nongraphene 2D material interacted with overgrown and substrate layers and also exhibited lattice transparency. The WGM cavity embedding monolayer MoS₂ showed enhanced luminescence of MoS₂ and multimodal emission.

KEYWORDS: remote epitaxy, microcavity, two-dimensional material, transition metal dichalcogenides, polarity inversion, whispering-gallery-mode



INTRODUCTION

A clean and abrupt interface at the atomic scale is important for materializing concepts of basic sciences and a prerequisite for manufacturing advanced devices. Two-dimensional (2D) materials provide opportunities to obtain atomically smooth interfaces with clear-cut composition profiles in various heterostructures, due to the absence of surface dangling bonds on the materials. 2D materials are essential building blocks of various heterostructures and conventional thin films, hereafter called 3D materials. Recent advances in 2D materials-based heterostructures have demonstrated emergent phenomena, such as twistrionics,^{1–3} interlayer excitons in 2D/2D,^{4–6} enhanced electromagnetic coupling in 2D/3D,⁷ and advanced manufacturing of 2D/3D devices.^{8–12}

Stacking and direct growth have been two fabrication approaches to embed 2D materials in heterostructures. Stacking 2D materials to fabricate heterostructures is widely used for 2D/2D and 2D/3D heterostructures. Although stacking of 2D materials has been successfully employed in diverse fields, it is difficult to avoid unintentional interfacial contamination during the preparation of individual 2D

materials in supporting media and during subsequent stacking.¹³ Moreover, stacking 2D materials is not appropriate for scalable fabrication of devices and architectures due to the formation of unintentional wrinkles and bubbles. Direct growth of 2D or 3D materials on other 2D and 3D materials has advantages over stacking. van der Waals (vdW) and remote epitaxy techniques have shown that 2D material-embedding heterostructures with clean and abrupt interfaces can be prepared in a manner compatible with mass production.^{12,14,15} Especially, remote epitaxy based on lattice transparency of an atomically thin 2D material is of great interest because the technique has high potential as a way to investigate the epitaxy mechanism across vdW gap, and for scalable and economical manufacturing of semiconductor devices.^{16–19} In principle,

Received: October 5, 2021

Accepted: February 1, 2022

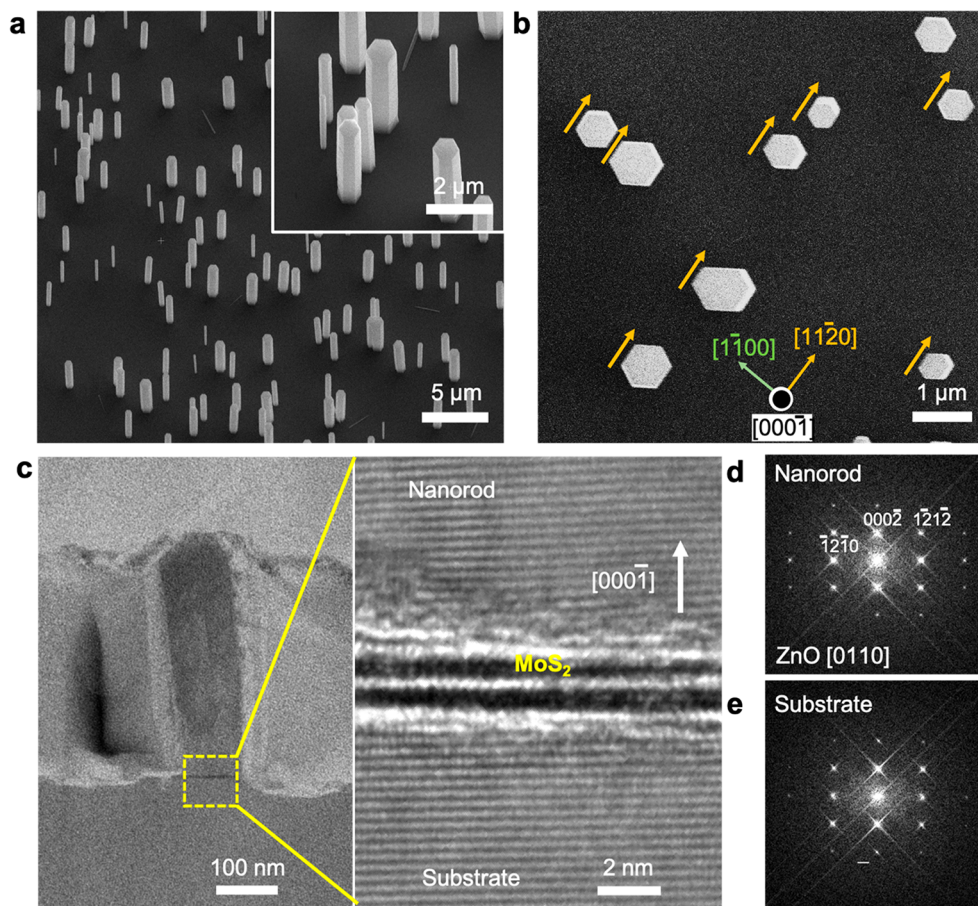


Figure 1. Remote epitaxy of ZnO NR on ZnO crystal across monolayer MoS₂. (a) Tilted view and (b) top view SEM images of ZnO NRs on MoS₂/ZnO. (c) Cross-sectional TEM image of ZnO NR/MoS₂/ZnO heterostructure. Selective area electron diffraction patterns of ZnO NR (d) and ZnO crystal (e).

remote epitaxy can be widely used because the absence of surface dangling bonds on a 2D material eliminates the problem of material incompatibility, a critical bottleneck of covalent and ionic bonding-based conventional epitaxy. Previous reports have established that remote epitaxy can be applied for various 3D materials.^{14,15,20,21} Nevertheless, the only 2D material that can currently be used as a substrate for remote epitaxy is graphene. Remote epitaxy on a nongraphene material has rarely been reported with indication of material degradation.²²

The major bottlenecks of remote epitaxy on nongraphene 2D materials are the decrease in lattice transparency and degradation of the 2D material under typical conditions of epitaxy involving chemical and physical vapor deposition techniques. The underlying principle of remote epitaxy is that the atomic arrangement of the overgrown layer on the 2D material is governed by the surface potential of the material beneath the 2D material. For remote interaction across a 2D material, its interaction with surrounding media should be minimized. Atomically thin single-element graphene with an extremely low dipole moment along the in-plane and out-of-plane directions is an ideal material for remote epitaxy. On the other hand, other 2D materials, such as transition metal dichalcogenides (TMDCs) and hexagonal boron nitride, have their own polarization field, which affects the potential of the layer underneath the 2D material.^{14,23} Thus, the lattice transparency of a nongraphene 2D material is significantly

lower than that of graphene. Moreover, a nongraphene 2D material is degraded in certain chemical environments. Although there have been reports that the integrity of certain TMDCs, such as MoS₂ and WS₂, can be preserved at elevated temperatures under vacuum or hydrogen atmosphere,^{24–26} atom diffusion resulting in vacancies and nonstoichiometry in a monolayer occurs in a reactive environment, which is common during epitaxy.²⁷

Remote epitaxy on a nongraphene 2D material can be accomplished by developing protocols resolving the bottlenecks described above. The lower lattice transparency can be overcome by material combination. The polarity principle of remote epitaxy implies that higher ionicity enhances potential penetration through a 2D material.^{23,28} Thus, potential penetration of a noncentrosymmetric material across a nongraphene 2D material may not be affected by polarization of the 2D material. Degradation of the 2D material during the remote epitaxy process can be minimized or prevented by careful selection of mild processing parameters, such as low temperature and nonharsh plasma condition.

Herein, we report remote epitaxy of ZnO on monolayer MoS₂. In contrast to previous remote epitaxy studies, which focused on manufacturing issues associated with 3D materials or exhibited degradation of the 2D material, our study demonstrates that individual 2D and 3D constituents can be integrated in one architecture. Analysis of the ZnO/MoS₂/ZnO architecture prepared by remote epitaxy revealed that the

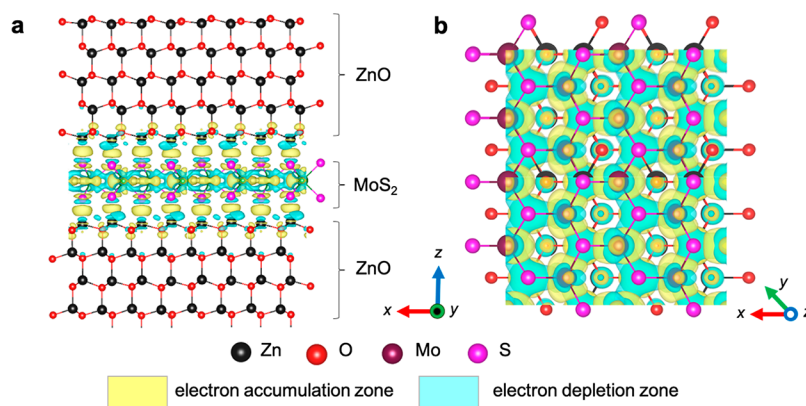


Figure 2. First-principles calculation of ZnO/MoS₂/ZnO. Side view (a) and top view (b) of atomic configuration and charge density distribution of ZnO/monolayer MoS₂/ZnO heterostructure.

luminescent characteristic of the monolayer MoS₂ was affected by a cavity made of the surrounding ZnO segments.

RESULTS AND DISCUSSION

Remote epitaxy of ZnO on monolayer MoS₂ was accomplished by hydrothermal synthesis of ZnO nanorods (NRs) on monolayer MoS₂/ZnO substrate. The continuous thin film of monolayer MoS₂ was grown on an SiO₂/Si substrate by metal–organic chemical vapor deposition (MOCVD). Details of the MoS₂ growth are described elsewhere.^{29,30} The MoS₂ was delaminated from the SiO₂ and subsequently transferred onto a *c*-oriented and Zn-terminated ZnO crystal. Figure 1a shows vertically aligned ZnO NRs on the transferred monolayer MoS₂ thin film. The top-view image (Figure 1b) reveals long-range ordering of sidewall {1010} facets of individual ZnO NRs over an area of 30 × 30 μm², which is significantly larger than the typical grain size of monolayer MoS₂ grown by MOCVD.^{29,31} However, the ZnO NRs were not evenly nucleated on the monolayer MoS₂. Most of ZnO NRs are adjacent to the nearest neighboring NRs within 2 and 3 μm which is comparable to the grain size of the monolayer MoS₂ in this study. The distance between NR clusters is in the range of 5 and 10 μm. The inhomogeneous distribution of ZnO NRs on the monolayer MoS₂ implies that there are favorable nucleation sites of ZnO NRs on the monolayer MoS₂ composed of multiple grains resulting in distribution of misalignment between ZnO and the MoS₂ with angles. Thorough understanding of effects of interlayer misalignment, represented by twist angles, on remote epitaxy is a crucial topic for follow-up study. The alignments of ZnO NRs along vertical and in-plane directions indicated that the ZnO NRs grown on monolayer MoS₂ were affected by the ZnO crystal underneath the MoS₂ layer. Cross-sectional transmission electron microscopy (X-TEM) revealed the epitaxial relationship between the overgrown ZnO NRs and the ZnO crystal across the monolayer MoS₂. To minimize damage and sputtering of the monolayer MoS₂ during the X-TEM sample preparation, focused ion beam milling and final thinning were conducted at the cryogenic temperature of 120 K. The high-resolution (HR) TEM image (Figure 1c) and electron diffraction patterns (Figure 1D,E) of the ZnO NR and ZnO crystal revealed that the two ZnO segments over and underneath the monolayer MoS₂ had an epitaxial relationship. The HRTEM images obtained in different focal planes (Figure S1) showed that the ZnO/MoS₂/ZnO had a single crystalline structure embedding

atomically thin MoS₂ without noticeable structural damage. The absence of a hole in the monolayer MoS₂ (Figure 1c and Figure S1) indicated that the epitaxial relationship between the ZnO NR and ZnO crystal was achieved through remote interaction, consistent with the principle of remote epitaxy. Tilt angles of the ZnO planes of the overgrown ZnO NR ranged from 0.2° to 1.0° across the interfacial plane (Figure S2). The tilt of the overgrown ZnO NRs relative to the ZnO crystal can be explained by miscutting of the ZnO crystal and warping of the transferred monolayer MoS₂.

The mechanism enabling the observed remote epitaxy of ZnO on monolayer MoS₂ was investigated from the perspective of energetics and charge density distribution, estimated by density functional theory (DFT) calculations incorporating geometrical relaxation through vdW interaction. From an energetic perspective, ZnO/MoS₂/ZnO should have atomic arrangements that minimize the system's energy with stable interfaces. The model system for the DFT calculations consisted of a ZnO bottom segment with four unit cells, monolayer MoS₂ at the central region, and a top ZnO segment with four unit cells. Both Zn- and O-terminated surfaces attached to the sandwiched monolayer MoS₂ were considered. A series of DFT calculations established that the ZnO/MoS₂/ZnO structure was stable when Zn atoms on the top and the bottom ZnO segments faced to the S atom layers of monolayer MoS₂ (Figure S3). In the case of the oxygen atom layer facing the S atom layer, either for the top or for the bottom ZnO segment, the whole ZnO/MoS₂/ZnO system became unstable, reflected in the excess energy of the system compared with the sum of the energies of the top and bottom ZnO segments and MoS₂. Stabilization of the ZnO/MoS₂/ZnO system with an O-terminated ZnO segment required distortion of the crystal structure of the O-terminated ZnO segment (Figure S3). The absence of a distorted ZnO crystal in Figure 1c indicates that the remote epitaxially grown ZnO/MoS₂/ZnO structure had a stable interface, defined by the atomic arrangement of O–Zn–S–Mo–S–Zn–O along the out-of-plane direction. The arrangement of electronegative S atoms and electropositive Zn atoms in a row was preferable from the perspective of energetics. However, the atomic arrangement implies polarity inversion between the top and the bottom ZnO segments. The possibility of polarity inversion, which has not been observed in previous studies of remote epitaxy on graphene, suggests that remote epitaxy on a nongraphene 2D material can be understood by considering multiple aspects of kinetics and

energetics beyond only lattice transparency, such as polarity control of III-nitride thin film growth.^{32,33}

The DFT-simulated atomic arrangement and charge density distribution are visualized in Figure 2. In the energy-minimizing atomic configuration of O–Zn–S–Mo–S–Zn–O along the out-of-plane direction, the side (Figure 2a) and top (Figure 2b) views show that the top and the bottom ZnO segments were epitaxially aligned. Figure 2a clearly shows that MoS₂-mediated charge transfer occurred between the top and the bottom ZnO segments. The spatial overlap of electron accumulation (yellow) and depletion (blue) regions depicted in the contour map of the charge distribution (Figure 2b) reveals that the ZnO segments separated by the monolayer MoS₂ had the same atomic arrangement in space, which supports remote interaction between the ZnO segments. The electron accumulation and depletion regions at the interface between the MoS₂ and upper ZnO layer mirrored those at the interface between the MoS₂ and lower ZnO layer. The mirror-symmetric charge distribution along the MoS₂ is consistent with the polarity inversion behavior shown in Figure S3. The MoS₂-mediated charge transfer was quantified by the adsorption energy of the top ZnO segment onto the MoS₂/ZnO heterostructure. The adsorption energy of the top ZnO layer onto the MoS₂/ZnO vdW heterostructure is $-88.52 \text{ meV}/\text{\AA}^2$, which is stronger than the estimated energy of $-55.5 \text{ meV}/\text{\AA}^2$ for the remote epitaxially grown ZnO on the graphene/GaN heterostructure.³⁴ The stronger interaction indicates that the monolayer MoS₂ facilitates stable remote epitaxial growth of ZnO through MoS₂-mediated charge transfer.

In the DFT calculations, in-plane piezoelectric field in the monolayer MoS₂, induced by lattice mismatch between ZnO and MoS₂, was not fully considered. Strong in-plane piezoelectric field in a crystalline single grain of monolayer MoS₂ under mechanical deformation has been reported.³⁵ Although remote epitaxy mechanism based on lattice transparency focuses on field penetration along out-of-plane direction, in-plane field distribution can agitate the substrate's potential distribution. However, the monolayer MoS₂ thin film utilized for the remote epitaxy in the study consists of multiple grains with different in-plane crystallographic orientations. Built-in strain in the whole MoS₂ thin film can be lower than that in an individual crystalline grain. In addition, vdW relaxation in a 2D/3D heterostructure mainly occurs in an overgrown layer not in a 2D material embedded in the heterostructure.³⁶ In our DFT calculation including vdW relaxation, the strain in the monolayer MoS₂ was less than 0.2%, which may not induce significant in-plane piezoelectric field.

The ZnO/MoS₂/ZnO heterostructure is considered to be a cavity made of monolayer TMDC surrounded by a dielectric medium. To utilize the remote epitaxy accomplished in this study, a cavity structure was fabricated. Figure 3a schematically illustrates the cavity fabrication procedure. After ZnO NRs were prepared on undoped GaN thin film, monolayer MoS₂ continuous thin film was transferred onto the ZnO NRs. The MoS₂ placed on top of the ZnO NRs remained in place. However, the MoS₂ regions outside the NR tops were torn and rinsed away. The MoS₂/ZnO NR vdW heterostructures were used as a substrate for the subsequent growth of ZnO NRs via hydrothermal synthesis. Figure 3b presents a schematic illustration and corresponding SEM images of the ZnO/MoS₂/ZnO NR heterostructures. Figure 3b shows that the top ZnO segments were selectively grown on the tops of the

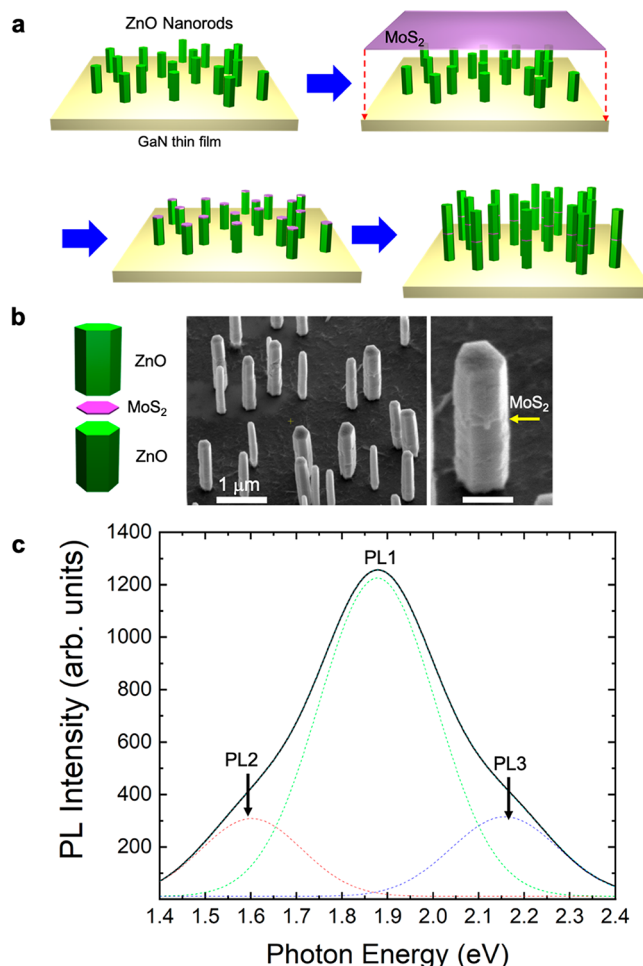


Figure 3. ZnO/MoS₂/ZnO NR heterostructures. (a) Schematic of the preparation of ZnO/MoS₂/ZnO NR heterostructures via remote epitaxy. (b) Exploded-view drawing and tilted view SEM images of a ZnO (green)/MoS₂ (violet)/ZnO (green) NR heterostructure. (c) RT μ -PL spectrum of a single ZnO/MoS₂/ZnO NR heterostructure with deconvoluted spectra labeled with PL1, PL2, and PL3.

MoS₂/ZnO NR heterostructures. No MoS₂ was present on the sidewalls of the ZnO NRs (Figure S4). Moreover, there was no rotation of the top ZnO segments with respect to the bottom ZnO segments. The alignment of sidewall facets between the top and the bottom ZnO segments is consistent with Figure 1a, indicating remote epitaxy of ZnO on MoS₂. The MoS₂ is located at the pinched points at the middle of the ZnO/MoS₂/ZnO NR heterostructures.

Room temperature microphotoluminescence (RT μ -PL) measurements were performed to characterize the optical properties of the ZnO/MoS₂/ZnO NR heterostructures. Before the MoS₂ and ZnO NRs were heterostructured, the RTPL spectra of monolayer MoS₂ thin film and ZnO NRs were obtained; their spectra did not overlap (Figure S5). The dominant PL emissions of the monolayer MoS₂ and the ZnO NRs were observed at 1.87 and 3.3 eV, respectively. The RTPL spectrum of the ZnO NRs showed weak emission at visible wavelengths in the range of 2 and 2.3 eV. Figure 3c shows the RT μ -PL spectrum of a single ZnO/MoS₂/ZnO NR heterostructure dispersed onto a 300 nm thick SiO₂/Si substrate. The origin of the dominant and strong PL emission at 1.9 eV is assigned to A excitons of monolayer MoS₂. The

observation of A excitonic emission from monolayer MoS₂ in the NR heterostructure indicates that the monolayer MoS₂ was not noticeably degraded during the hydrothermal synthesis of ZnO NRs on the transferred MoS₂. Monolayer MoS₂ is known as a stable material over several days in an aqueous environment at 75 °C.³⁷ Degradation of monolayer MoS₂ during the growth of ZnO NRs at 95 °C for 4 h is not noticeable. The full-width at half-maximum (FWHM) of the RT μ -PL spectrum in Figure 3c is 320 meV, which is remarkably larger than the FWHM (52 meV) of the RTPL spectrum of the monolayer MoS₂ thin film in Figure S5. The FWHM difference originates from the intensity of the excitation source. In the PL studies, the excitation intensities of the RTPL (for MoS₂) and the RT μ -PL (for the ZnO/MoS₂/ZnO heterostructure) measurements were 1 and 125 kW/cm², respectively. Previous reports on power-dependent PL studies of monolayer MoS₂ showed spectral broadening with increasing excitation intensity.³⁸ The RT time-resolved (TR) PL spectrum (Figure S6) was fitted by biexponential decay curves. The fast and the slow PL decay constants of the 1.9 eV emission were 0.5 and 7 ns, respectively, comparable to the values which reported by of monolayer MoS₂ TRPL studies.^{39,40} The average PL decay constant of the 1.9 eV emission was 500 ps. Meanwhile, the reported PL decay constant of defect emission of ZnO at visible wavelengths exceeds 5 ns.⁴¹ The dominant PL emission peak and the PL decay constant support that the monolayer MoS₂ was not degraded during the remote epitaxy process. The PL mapping at 1.9 eV of individual ZnO/MoS₂/ZnO heterostructures (Figure S7) shows that the MoS₂ PL emission occurred in the entire heterostructure though the monolayer MoS₂ located at the middle of the heterostructure. The omnipresent PL emission at 1.9 eV in spatially resolved PL is attributed to the ZnO surrounding medium acting either as a waveguide delivering the excitation laser to the monolayer MoS₂ or as a microcavity confining the PL of the monolayer MoS₂.

Another spectral feature shown in Figure 3c is the appearance of two shoulders at 1.6 (PL2) and 2.16 (PL3) eV with the same spacing of 280 meV from the center emission at 1.88 eV (PL1), as shown in the deconvoluted RT μ -PL spectrum (dotted line). PL2 and PL3 do not correspond to known excitonic emissions of monolayer MoS₂. Moreover, the equidistant energy levels of PL2 and PL3 from PL1 indicate that PL2 and PL3 are modal emissions of PL1. The well-faceted hexagonal structure of ZnO, surrounding the monolayer MoS₂, can be considered as a whispering-gallery-mode (WGM) cavity.

In addition to the spectral features discussed above, it is worthwhile to mention that formation of the ZnO/MoS₂/ZnO heterostructure was useful to protect the embedded monolayer MoS₂. The RT PL emission spectra of a pristine monolayer MoS₂ grown by MOCVD and the embedded MoS₂ in ZnO/MoS₂/ZnO heterostructure were compared after storing the samples in atmospheric condition for 6 months. The RTPL of the pristine monolayer MoS₂ disappeared after 6 months. On the other hand, the RTPL of the embedded MoS₂ in ZnO/MoS₂/ZnO heterostructure was preserved without noticeable degradation.

Cathodoluminescence (CL) microscopy was used to study waveguide and cavity effects in a single ZnO/MoS₂/ZnO heterostructure. CL microscopy offers high spatial resolution and excitation of both ZnO and MoS₂. Figure 4a presents the RT CL spectrum and monochromatic CL mapping at several

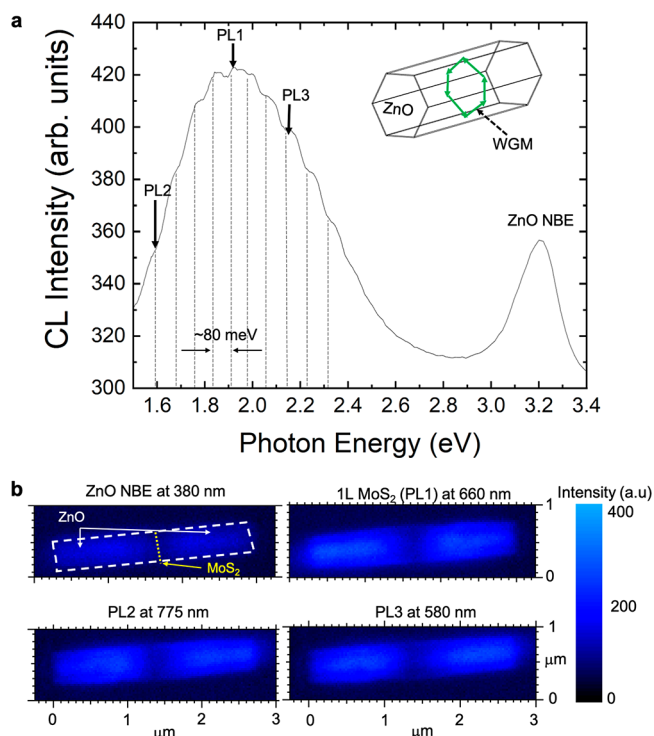


Figure 4. Cathodoluminescent characteristics of a ZnO/MoS₂/ZnO NR heterostructure. (a) RTCL spectrum of a single ZnO/MoS₂/ZnO NR heterostructure. (b) Monochromatic CL images of a ZnO/MoS₂/ZnO NR heterostructure, obtained at 380, 580, 660, and 775 nm. The white dashed line guides the region of a ZnO/MoS₂/ZnO NR heterostructure.

wavelengths of a single ZnO/MoS₂/ZnO NR heterostructure dispersed on a 300 nm thick SiO₂/Si substrate. The ZnO near-band-edge emission (NBE) at 380 nm (3.26 eV) and multiple emission peaks in the broad spectral range from 500 to 800 nm were observed. The center wavelength of the broad emission at visible wavelengths was 660 nm (1.88 eV), corresponding to the dominant PL emission from monolayer MoS₂ shown in Figure 3c and Figure S5. The CL emission at 660 nm was not observed from a top ZnO segment delaminated from a ZnO NR/MoS₂/ZnO NR heterostructure during dispersion of the heterostructures onto a SiO₂/Si substrate. Multiple peaks with equidistant energy levels of 80 meV were also observed in the RT CL spectrum. The CL emission intensity of the monolayer MoS₂ was stronger than that of the ZnO NRs although the volume of the monolayer MoS₂ in the NR heterostructure was negligibly small. The dominant CL emission from the MoS₂ implied enhancement of emission from the MoS₂. WGM-enhanced emission provides a mechanism consistent with the observations. For the hexagonal WGM cavity, the constructive interference condition can be estimated as follows:⁴²

$$nR = \frac{\lambda}{3\sqrt{3}} \left[N + \frac{6}{\pi} \arctan(\beta\sqrt{3n^2 - 4}) \right] \quad (1)$$

where n is the refractive index of ZnO, R is the side length of the hexagonal cavity, λ is the wavelength of light, N is the resonance interference order, and β is the inverse of n for the polarization mode. The estimated emission wavelengths, including the CL emissions labeled as PL2 and PL3, fitted to the multiple peaks in Figure 4A.

Figure 4b shows monochromatic CL images at 380 (ZnO NBE, 3.26 eV), 660 (PL1, 1.88 eV), 775 (PL2, 1.6 eV), and 580 (PL3, 2.13 eV) nm. All monochromatic CL emissions were observed through the entire ZnO/MoS₂/ZnO NR heterostructure. The omnipresent CL emission of PL1, PL2, and PL3 indicated that the MoS₂ was excited regardless of the electron beam position on the single ZnO/MoS₂/ZnO NR heterostructure. Electrons having 5 kV acceleration voltage excited the ZnO NR. The excitation generated excitons and subsequent excitonic recombination, resulting in an energy of 3.28 eV. Because the typical diffusion length of excitons in ZnO is shorter than 250 nm at cryogenic temperatures,^{43,44} funneling ZnO excitons into the monolayer MoS₂ cannot explain the MoS₂ CL emission in the 3 μm range. In the WGM cavity, the ZnO NBE light could reach to the monolayer MoS₂ via the waveguide effect and induce subsequent excitation of the monolayer MoS₂. The lower monochromatic CL intensity in the region near the embedded MoS₂ can be explained by the narrower diameter in the region as shown in Figure 3b, inducing light leakage and deviation of the region from the focal plane of the parabolic mirror to collect emitted light in the CL measurement system.

CONCLUSION

We realized remote epitaxy of a 3D material with strong ionicity (ZnO) on a nongraphene 2D material (monolayer MoS₂). DFT calculations revealed that the nongraphene 2D material induced changes in the potential of the substrate material, indicated by polarity inversion. The interaction between the substrate material and the nongraphene 2D material implies another role of the 2D material substrate besides lattice transparency. Remote epitaxy of ZnO on monolayer MoS₂ was used to materialize a platform for many-body physics. The individual ZnO/MoS₂/ZnO NR heterostructure behaved as a WGM cavity, which is a widely utilized for exciton–polariton studies. Our architecture provided a clean and abrupt interface in a combination of incommensurate materials, and our findings enable the extension of remote epitaxy from basic science to advanced manufacturing.

EXPERIMENTAL METHODS

Transfer of Monolayer MoS₂ onto ZnO. Monolayer MoS₂ thin film grown on SiO₂/Si substrate was covered with poly(methyl methacrylate) (PMMA, MicroChem 495 K A4) by spin coating (spinning at 3000 rpm for 30 s). The PMMA-coated MoS₂/SiO₂/Si substrate was dipped in potassium hydroxide (KOH) aqueous solution to etch SiO₂ layer for 30 s. The floated PMMA/MoS₂ membrane was moved to deionized (DI) water. Subsequently, the PMMA/MoS₂ membrane was transferred onto a ZnO crystal or ZnO NRs. Poor adhesion of MoS₂ resulted in delamination of MoS₂ during ZnO NR growth. To improve adhesion between the transferred MoS₂ and ZnO, the PMMA/MoS₂/ZnO sample was dried at 70 °C for 8 h on a hot plate. The PMMA layer was removed by immersion in acetone for 30 min. After the transfer procedure, the MoS₂/ZnO samples were dried by nitrogen blowing.

Remote Epitaxy of ZnO on MoS₂. The synthesized monolayer MoS₂ was transferred onto a ZnO crystal or a sample of ZnO NRs using a poly(methyl methacrylate) layer. ZnO NRs were grown by hydrothermal method on the transferred MoS₂/ZnO sample in a Teflon-lined autoclave. The nutrient solution was prepared by dissolving 25 mM zinc nitrate hexahydrate, 25 mM hexamethylenetetramine, and 5 mM polyethylenimine in deionized water. The hydrothermal synthesis was performed at 95 °C.

Sample Preparation for Cross-Sectional Transmission Electron Microscopy. The sample preparation was performed on

a Scios 2 Dual Beam SEM/focused ion beam (FIB) with a Leica VCT cryogenic stage installed. To preserve the structural integrity of the monolayer MoS₂ layer and reduce artifact inclusion, the sample was cooled to 120 K and Ga ion FIB milling was performed with a reduced accelerating voltage of 16 kV. Final thinning was carried out using a beam current of 50 pA.

Photoluminescence Characterization of Single Nanostructures. After dispersion of the nanostructures, the dispersed NRs and ZnO/MoS₂/ZnO NR heterostructures on SiO₂/Si substrates were loaded onto a home-built confocal laser microscope. A pulsed diode laser with a wavelength of 375 nm was focused onto the samples by a microscopy objective (40×, NA = 0.95). PL from a single nanostructure was collected by the same objective, cleaned up by long-pass filters, and sent to a spectrometer equipped with a charge-coupled device camera or to single photon avalanche diodes.

Cathodoluminescence Characterization. Dispersed ZnO/MoS₂/ZnO NR heterostructures on a SiO₂/Si substrate were loaded into a SEM-CL system (Attolight Allain CL-SEM4027). The acceleration voltage and the beam current were 5 kV and 9 nA, respectively. The CL data was acquired using a fast Si CMOS camera.

DFT Calculation Methods. The DFT calculations were performed using the planewave pseudopotential code VASP^{45–47} under the generalized gradient approximation of Perdew, Burke, and Ernzerhof (PBE).⁴⁸ For atomic core levels, we have used projected augmented wave (PAW) potentials treating the 2s2p of O, 4s3d of Zn, 3s3p of S, and 4p5s4d of Mo as the explicit valence electrons. A maximum energy cutoff of 400 eV is used for plane-wave basis set. We performed full geometrical relaxation incorporating vdW interaction and calculated the charge density difference. Our unit cells contain the MoS₂/ZnO composite and ZnO/MoS₂/ZnO composite, which also includes a vacuum layer. To incorporate the vdW interaction, we have used the optB86bvdW functional, where the exchange functional was optimized for the correlation part.⁴⁹ Therefore, the LDA correlation part present in the PBE functional is removed by using the parameter AGGAC = 0.000 in the input file in order to avoid double-counting. We used 3 × 3 × 1 k points in the first Brillouin zone (BZ) for our ionic relaxation and energy minimization calculations.

ASSOCIATED CONTENT

Supporting Information

The Supporting Information is available free of charge at <https://pubs.acs.org/doi/10.1021/acsnano.1c08779>.

Cross-sectional TEM images of ZnO NR/MoS₂/ZnO crystal, obtained in different focal planes; diagram of overlapped electron diffraction patterns obtained from ZnO NR and ZnO crystal; schematic illustration of simulated ZnO crystal structure in ZnO/MoS₂/ZnO in the case of the Zn-face adjacent to the S atom layer of MoS₂; low magnification cross-sectional TEM images of remote epitaxial ZnO NR/MoS₂/ZnO crystal; RTPL spectra of as-prepared monolayer MoS₂ and a single ZnO NR; RT TRPL spectrum of the 1.9 eV emission of a single ZnO/MoS₂/ZnO NR heterostructure; monochromatic PL image (1.9–2.2 eV) of the ZnO/MoS₂/ZnO NR heterostructures dispersed onto a SiO₂/Si substrate; RT CL spectrum of a detached ZnO segment (PDF)

AUTHOR INFORMATION

Corresponding Author

Jinkyung Yoo – Center for Integrated Nanotechnologies, Los Alamos National Laboratory, Los Alamos, New Mexico 87545, United States; orcid.org/0000-0002-9578-6979; Email: jyoo@lanl.gov

Authors

Yeonhoo Kim – Center for Integrated Nanotechnologies, Los Alamos National Laboratory, Los Alamos, New Mexico 87545, United States; Present Address: Interdisciplinary Materials Measurement Institute, Korea Research Institute of Standards and Science (KRISS), Daejeon 34133, Republic of Korea

John Watt – Center for Integrated Nanotechnologies, Los Alamos National Laboratory, Los Alamos, New Mexico 87545, United States

Xuedan Ma – Center for Nanoscale Materials, Argonne National Laboratory, Lemont, Illinois 50439, United States; orcid.org/0000-0002-3163-1249

Towfiq Ahmed – T-4, Los Alamos National Laboratory, Los Alamos, New Mexico 87545, United States; orcid.org/0000-0002-3964-7763

Suhyun Kim – Department of Materials Science and Engineering, Korea Advanced Institute of Science and Technology (KAIST), Daejeon 34141, Republic of Korea

Kibum Kang – Department of Materials Science and Engineering, Korea Advanced Institute of Science and Technology (KAIST), Daejeon 34141, Republic of Korea; orcid.org/0000-0003-1674-1826

Ting S. Luk – Center for Integrated Nanotechnologies, Sandia National Laboratories, Albuquerque, New Mexico 87185, United States

Young Joon Hong – Department of Nanotechnology and Advanced Materials Engineering, Sejong University, Seoul 05006, Republic of Korea; orcid.org/0000-0002-1831-8004

Complete contact information is available at:
<https://pubs.acs.org/10.1021/acsnano.1c08779>

Author Contributions

J.Y. conceived and directed the main experimental idea and performed cathodoluminescence measurements and analyses. Y.K. conducted synthesis of the heterostructures and electron microscopy observations. J.W. conducted cryo-FIB, TEM observation, and analyses. X.M. performed microphotoluminescence measurements. T.A. conducted theoretical simulations. S.K. prepared monolayer MoS₂ thin films. T.S.L. performed photoluminescence measurements of ZnO NRs. K.K. and Y.J.H. analyzed the structural and luminescent characteristics. J.Y. is responsible for all research results. J.Y. and Y.K. cowrote the manuscript. All authors discussed and commented on the manuscript.

Notes

The authors declare no competing financial interest.

ACKNOWLEDGMENTS

This research was financially supported by the Laboratory Directed Research and Development program of Los Alamos National Laboratory (20190224ER). This work was partly performed at CINT, a U.S. Department of Energy, office of Basic Energy Sciences User Facility at Los Alamos National Laboratory (Contract 89233218CNA000001) and Sandia National Laboratories (Contract DE-NA-0003525). This work was also performed, in part, at the Center for Nanoscale Materials, a U.S. Department of Energy, office of Basic Energy Science User Facility, and supported by the U.S. Department of Energy, Office of Science, under Contract No. DE-AC02-06CH11357.

REFERENCES

- (1) Cao, Y.; Fatemi, V.; Fang, S.; Watanabe, K.; Taniguchi, T.; Kaxiras, E.; Jarillo-Herrero, P. Unconventional superconductivity in magic-angle graphene superlattices. *Nature* **2018**, *556* (7699), 43–50.
- (2) Carr, S.; Fang, S.; Kaxiras, E. Electronic-structure methods for twisted moire layers. *Nat. Rev. Mater.* **2020**, *5* (10), 748–763.
- (3) Guo, H. W.; Hu, Z.; Liu, Z. B.; Tian, J. G. Stacking of 2D Materials. *Adv. Funct. Mater.* **2021**, *31* (4), 2007810.
- (4) Rivera, P.; Schaibley, J. R.; Jones, A. M.; Ross, J. S.; Wu, S. F.; Aivazian, G.; Klement, P.; Seyler, K.; Clark, G.; Ghimire, N. J.; Yan, J. Q.; Mandrus, D. G.; Yao, W.; Xu, X. D. Observation of long-lived interlayer excitons in monolayer MoSe₂-WSe₂ heterostructures. *Nat. Commun.* **2015**, *6*, 6242.
- (5) Zhu, X. Y.; Monahan, N. R.; Gong, Z. Z.; Zhu, H. M.; Williams, K. W.; Nelson, C. A. Charge Transfer Excitons at van der Waals Interfaces. *J. Am. Chem. Soc.* **2015**, *137* (26), 8313–8320.
- (6) Liu, Y. D.; Fang, H. L.; Rasmita, A.; Zhou, Y.; Li, J. T.; Yu, T.; Xiong, Q. H.; Zheludev, N.; Liu, J.; Gao, W. B. Room temperature nanocavity laser with interlayer excitons in 2D heterostructures. *Sci. Adv.* **2019**, *5* (4), No. eaav4506.
- (7) Kum, H. S.; Lee, H.; Kim, S.; Lindemann, S.; Kong, W.; Qiao, K.; Chen, P.; Irwin, J.; Lee, J. H.; Xie, S.; Subramanian, S.; Shim, J.; Bae, S.-H.; Choi, C.; Ranno, L.; Seo, S.; Lee, S.; Bauer, J.; Li, H.; Lee, K.; Robinson, J. A.; Ross, C. A.; Schlom, D. G.; Rzchowski, M. S.; Eom, C.-B.; Kim, J. Heterogeneous integration of single-crystalline complex-oxide membranes. *Nature* **2020**, *578* (7793), 75–81.
- (8) Han, N.; Viet Cuong, T.; Han, M.; Deul Ryu, B.; Chandramohan, S.; Bae Park, J.; Hye Kang, J.; Park, Y.-J.; Bok Ko, K.; Yun Kim, H.; Kyu Kim, H.; Hyoung Ryu, J.; Katharria, Y. S.; Choi, C.-J.; Hong, C.-H. Improved heat dissipation in gallium nitride light-emitting diodes with embedded graphene oxide pattern. *Nat. Commun.* **2013**, *4* (1), 1452.
- (9) Ayari, T.; Sundaram, S.; Li, X.; El Gmili, Y.; Voss, P. L.; Salvestrini, J. P.; Ougazzaden, A. Wafer-scale controlled exfoliation of metal organic vapor phase epitaxy grown InGaN/GaN multi quantum well structures using low-tack two-dimensional layered h-BN. *Appl. Phys. Lett.* **2016**, *108* (17), 171106.
- (10) Bitla, Y.; Chen, C.; Lee, H.-C.; Do, T. H.; Ma, C.-H.; Qui, L. V.; Huang, C.-W.; Wu, W.-W.; Chang, L.; Chiu, P.-W.; Chu, Y.-H. Oxide Heteroepitaxy for Flexible Optoelectronics. *ACS Appl. Mater. Interfaces* **2016**, *8* (47), 32401–32407.
- (11) Bae, S.-H.; Zhou, X.; Kim, S.; Lee, Y. S.; Cruz, S. S.; Kim, Y.; Hannon, J. B.; Yang, Y.; Sadana, D. K.; Ross, F. M.; Park, H.; Kim, J. Unveiling the carrier transport mechanism in epitaxial graphene for forming wafer-scale, single-domain graphene. *Proc. Natl. Acad. Sci. U.S.A.* **2017**, *114* (16), 4082–4086.
- (12) Bae, S.-H.; Kum, H.; Kong, W.; Kim, Y.; Choi, C.; Lee, B.; Lin, P.; Park, Y.; Kim, J. Integration of bulk materials with two-dimensional materials for physical coupling and applications. *Nat. Mater.* **2019**, *18* (6), 550–560.
- (13) Haigh, S. J.; Gholinia, A.; Jalil, R.; Romani, S.; Britnell, L.; Elias, D. C.; Novoselov, K. S.; Ponomarenko, L. A.; Geim, A. K.; Gorbachev, R. Cross-sectional imaging of individual layers and buried interfaces of graphene-based heterostructures and superlattices. *Nat. Mater.* **2012**, *11* (9), 764–767.
- (14) Kim, Y.; Cruz, S. S.; Lee, K.; Alawode, B. O.; Choi, C.; Song, Y.; Johnson, J. M.; Heidelberger, C.; Kong, W.; Choi, S.; Qiao, K.; Almansouri, I.; Fitzgerald, E. A.; Kong, J.; Kolpak, A. M.; Hwang, J.; Kim, J. Remote epitaxy through graphene enables two-dimensional material-based layer transfer. *Nature* **2017**, *544* (7650), 340–343.
- (15) Jeong, J.; Wang, Q.; Cha, J.; Jin, D. K.; Shin, D. H.; Kwon, S.; Kang, B. K.; Jang, J. H.; Yang, W. S.; Choi, Y. S. Remote heteroepitaxy of GaN microrod heterostructures for deformable light-emitting diodes and wafer recycle. *Sci. Adv.* **2020**, *6* (23), No. eaaz5180.
- (16) Lee, C.-H.; Kim, Y.-J.; Hong, Y. J.; Jeon, S.-R.; Bae, S.; Hong, B. H.; Yi, G.-C. Flexible Inorganic Nanostructure Light-Emitting Diodes Fabricated on Graphene Films. *Adv. Mater.* **2011**, *23* (40), 4614–4619.

- (17) Ayari, T.; Bishop, C.; Jordan, M. B.; Sundaram, S.; Li, X.; Alam, S.; ElGmili, Y.; Patriarche, G.; Voss, P. L.; Salvestrini, J. P.; Ougazzaden, A. Gas sensors boosted by two-dimensional h-BN enabled transfer on thin substrate foils: towards wearable and portable applications. *Sci. Rep.* **2017**, *7*, 15212.
- (18) Oh, H.; Park, J.; Choi, W.; Kim, H.; Tchoe, Y.; Agrawal, A.; Yi, G.-C. Vertical ZnO Nanotube Transistor on a Graphene Film for Flexible Inorganic Electronics. *Small* **2018**, *14* (17), 1800240.
- (19) Karrakchou, S.; Sundaram, S.; Gujrati, R.; Vuong, P.; Mballo, A.; Adjmi, H. E.; Ottapilakkal, V.; El Huni, W.; Bouzid, K.; Patriarche, G.; Ahaitouf, A.; Voss, P. L.; Salvestrini, J. P.; Ougazzaden, A. Monolithic Free-Standing Large-Area Vertical III-N Light-Emitting Diode Arrays by One-Step h-BN-Based Thermomechanical Self-Lift-Off and Transfer. *ACS Appl. Electron. Mater.* **2021**, *3* (6), 2614–2621.
- (20) Chae, S.; Jang, S.; Choi, W. J.; Kim, Y. S.; Chang, H.; Lee, T. I.; Lee, J.-O. Lattice Transparency of Graphene. *Nano Lett.* **2017**, *17* (3), 1711–1718.
- (21) Kim, H.; Lu, K.; Liu, Y.; Kum, H. S.; Kim, K. S.; Qiao, K.; Bae, S.-H.; Lee, S.; Ji, Y. J.; Kim, K. H.; Paik, H.; Xie, S.; Shin, H.; Choi, C.; Lee, J. H.; Dong, C.; Robinson, J. A.; Lee, J.-H.; Ahn, J.-H.; Yeom, G. Y.; Schlom, D. G.; Kim, J. Impact of 2D–3D Heterointerface on Remote Epitaxial Interaction through Graphene. *ACS Nano* **2021**, *15* (6), 10587–10596.
- (22) Ma, C.-H.; Lu, L.-S.; Song, H.; Chen, J.-W.; Wu, P.-C.; Wu, C.-L.; Huang, R.; Chang, W.-H.; Chu, Y.-H. Remote growth of oxide heteroepitaxy through MoS₂. *APL Mater.* **2021**, *9* (5), 051115.
- (23) Kong, W.; Li, H.; Qiao, K.; Kim, Y.; Lee, K.; Nie, Y.; Lee, D.; Osadchy, T.; Molnar, R. J.; Gaskill, D. K.; Myers-Ward, R. L.; Daniels, K. M.; Zhang, Y.; Sundram, S.; Yu, Y.; Bae, S.-h.; Rajan, S.; Shao-Horn, Y.; Cho, K.; Ougazzaden, A.; Grossman, J. C.; Kim, J. Polarity governs atomic interaction through two-dimensional materials. *Nat. Mater.* **2018**, *17* (11), 999–1004.
- (24) Eda, G.; Yamaguchi, H.; Voiry, D.; Fujita, T.; Chen, M.; Chhowalla, M. Photoluminescence from Chemically Exfoliated MoS₂. *Nano Lett.* **2011**, *11* (12), 5111–5116.
- (25) Xie, M. Z.; Zhou, J. Y.; Ji, H.; Ye, Y.; Wang, X.; Jiang, K.; Shang, L. Y.; Hu, Z. G.; Chu, J. H. Annealing effects on sulfur vacancies and electronic transport of MoS₂ films grown by pulsed-laser deposition. *Appl. Phys. Lett.* **2019**, *115* (12), 121901.
- (26) Jia, Z. Y.; Dong, J. Y.; Liu, L. X.; Nie, A. M.; Xiang, J. Y.; Wang, B. C.; Wen, F. S.; Mu, C. P.; Zhao, Z. S.; Xu, B.; Gong, Y. J.; Tian, Y. J.; Liu, Z. Y. Photoluminescence and Raman Spectra Oscillations Induced by Laser Interference in Annealing-Created Monolayer WS₂ Bubbles. *Adv. Opt. Mater.* **2019**, *7* (8), 1801373.
- (27) Lin, Y.-C.; Bilgin, I.; Ahmed, T.; Chen, R.; Pete, D.; Kar, S.; Zhu, J.-X.; Gupta, G.; Mohite, A.; Yoo, J. Charge transfer in crystalline germanium/monolayer MoS₂ heterostructures prepared by chemical vapor deposition. *Nanoscale* **2016**, *8* (44), 18675–18681.
- (28) Yoo, J.; Ahmed, T.; Chen, R.; Chen, A.; Kim, Y. H.; Kwon, K. C.; Park, C. W.; Kang, H. S.; Jang, H. W.; Hong, Y. J.; Yang, W. S.; Lee, C.-H. Enhanced nucleation of germanium on graphene via dipole engineering. *Nanoscale* **2018**, *10* (12), 5689–5694.
- (29) Kang, K.; Xie, S.; Huang, L.; Han, Y.; Huang, P. Y.; Mak, K. F.; Kim, C.-J.; Muller, D.; Park, J. High-mobility three-atom-thick semiconducting films with wafer-scale homogeneity. *Nature* **2015**, *520* (7549), 656–660.
- (30) Geum, D.-M.; Kim, S.; Khym, J.; Lim, J.; Kim, S.; Ahn, S.-Y.; Kim, T. S.; Kang, K.; Kim, S. Arrayed MoS₂–In_{0.53}Ga_{0.47}As van der Waals Heterostructure for High-Speed and Broadband Detection from Visible to Shortwave-Infrared Light. *Small* **2021**, *17* (17), 2007357.
- (31) Chowdhury, S.; Roy, A.; Liu, C.; Alam, M. H.; Ghosh, R.; Chou, H.; Akinwande, D.; Banerjee, S. K. Two-Step Growth of Uniform Monolayer MoS₂ Nanosheets by Metal–Organic Chemical Vapor Deposition. *ACS Omega* **2021**, *6* (15), 10343–10351.
- (32) Ramachandran, V.; Feenstra, R. M.; Sarney, W. L.; Salamanca-Riba, L.; Northrup, J. E.; Romano, L. T.; Greve, D. W. Inversion of wurtzite GaN(0001) by exposure to magnesium. *Appl. Phys. Lett.* **1999**, *75* (6), 808–810.
- (33) Northrup, J. E. Magnesium incorporation at (0001) inversion domain boundaries in GaN. *Appl. Phys. Lett.* **2003**, *82* (14), 2278–2280.
- (34) Jeong, J.; Min, K.-A.; Kang, B. K.; Shin, D. H.; Yoo, J.; Yang, W. S.; Lee, S. W.; Hong, S.; Hong, Y. J. Remote heteroepitaxy across graphene: Hydrothermal growth of vertical ZnO microrods on graphene-coated GaN substrate. *Appl. Phys. Lett.* **2018**, *113* (23), 233103.
- (35) Wu, W.; Wang, L.; Li, Y.; Zhang, F.; Lin, L.; Niu, S.; Chenet, D.; Zhang, X.; Hao, Y.; Heinz, T. F.; Hone, J.; Wang, Z. L. Piezoelectricity of single-atomic-layer MoS₂ for energy conversion and piezotronics. *Nature* **2014**, *514*, 470–474.
- (36) Bae, S.-H.; Lu, K.; Han, Y.; Kim, S.; Qiao, K.; Choi, C.; Nie, Y.; Kim, H.; Kum, H. S.; Chen, P.; Kong, W.; Kang, B.-S.; Kim, C.; Lee, J.; Baek, Y.; Shim, J.; Park, J.; Joo, M.; Muller, D. A.; Lee, K.; Kim, J. Graphene-assisted spontaneous relaxation toward dislocation-free heteroepitaxy. *Nat. Nanotechnol.* **2020**, *15*, 272–276.
- (37) Chen, X.; Shinde, S. M.; Dhakal, K. P.; Lee, S. W.; Kim, H.; Lee, Z.; Ahn, J.-H. Degradation behaviors and mechanisms of MoS₂ crystals relevant to bioabsorbable electronics. *NPG Asia Mater.* **2018**, *10*, 810–820.
- (38) Kaplan, D.; Gong, Y.; Mills, K.; Swaminathan, V.; Ajayan, P. M.; Shirodkar, S.; Kaxiras, E. Excitation intensity dependence of photoluminescence from monolayers of MoS₂ and WS₂/MoS₂ heterostructures. *2D Mater.* **2016**, *3* (1), 015005.
- (39) Lien, D.-H.; Uddin, S. Z.; Yeh, M.; Amani, M.; Kim, H.; Ager, J. W., III; Yablonovitch, E.; Javey, A. Electrical suppression of all nonradiative recombination pathways in monolayer semiconductors. *Science* **2019**, *364* (6439), 468–471.
- (40) Li, H.; Zhang, X. H. Temperature-dependent photoluminescence and time-resolved photoluminescence study of monolayer molybdenum disulfide. *Opt. Mater.* **2020**, *107*, 110150.
- (41) Han, N. S.; Shim, H. S.; Seo, J. H.; Kim, S. Y.; Park, S. M.; Song, J. K. Defect states of ZnO nanoparticles: Discrimination by time-resolved photoluminescence spectroscopy. *J. Appl. Phys.* **2010**, *107* (8), 084306.
- (42) Nobis, T.; Kaidashev, E. M.; Rahm, A.; Lorenz, M.; Grundmann, M. Whispering Gallery Modes in Nanosized Dielectric Resonators with Hexagonal Cross Section. *Phys. Rev. Lett.* **2004**, *93* (10), 103903.
- (43) Yoo, J.; Yi, G.-C.; Dang, L. S. Probing Exciton Diffusion in Semiconductors Using Semiconductor-Nanorod Quantum Structures. *Small* **2008**, *4* (4), 467–470.
- (44) Yoo, J.; Chon, B.; Tang, W.; Joo, T.; Dang, L. S.; Yi, G.-C. Excitonic origin of enhanced luminescence quantum efficiency in MgZnO/ZnO coaxial nanowire heterostructures. *Appl. Phys. Lett.* **2012**, *100* (22), 223103.
- (45) Kresse, G.; Hafner, J. Ab initio molecular dynamics for liquid metals. *Phys. Rev. B* **1993**, *47* (1), 558–561.
- (46) Kresse, G.; Furthmüller, J. Efficient iterative schemes for ab initio total-energy calculations using a plane-wave basis set. *Phys. Rev. B* **1996**, *54* (16), 11169–11186.
- (47) Kresse, G.; Furthmüller, J. Efficiency of ab-initio total energy calculations for metals and semiconductors using a plane-wave basis set. *Comput. Mater. Sci.* **1996**, *6* (1), 15–50.
- (48) Perdew, J. P.; Burke, K.; Ernzerhof, M. Generalized Gradient Approximation Made Simple. *Phys. Rev. Lett.* **1996**, *77* (18), 3865–3868.
- (49) Klimeš, J.; Bowler, D. R.; Michaelides, A. Van der Waals density functionals applied to solids. *Phys. Rev. B* **2011**, *83* (19), 195131.